# On the fracture response of shape memory alloys by void growth and coalescence

J. Makkar<sup>a</sup>, T. Baxevanis<sup>a,\*</sup>

<sup>a</sup>Department of Mechanical Engineering, University of Houston, Houston, TX 77204-4006, USA

#### Abstract

Although Shape Memory Alloys (SMAs) belong to a relatively brittle class of materials, that of intermetallics, their fracture surfaces are characterized by both cleavage and dimples, with the latter being indicative of ductile rupture. Two clear differentiators of SMAs from other intermetallics, which may contribute to the presence of ductile rupture are their ability to transform their crystallographic structure and the presence of precipitates in large volume fractions. In this paper, unit cell simulations are employed in an effort to quantify the relative importance of the two fracture mechanisms in the overall failure response of these materials. The numerical simulations involve a single pre-existing void, assumed to have initiated from a second phase particle, embedded in a SMA matrix material. Thus, the unit cell studies allow for an investigation of void growth and coalescence, ignoring void formation and its footprint in the subsequent microstructure evolution. The numerical studies show that void growth is rather limited before the peak stress-value in the effective stress-effective strain response of the unit cell for initial void-volume fractions representative of precipitation-hardened SMAs. Given the available experimental observations on notched round bars, which indicate that precipitation-hardened SMAs fail in a stress-controlled manner, the numerical studies suggest that void growth and coalescence should play a minor role in the formation of dimples, as compared to that of void nucleation and cleavage, and in turn into the fracture response of precipitated SMAs.

Keywords: shape memory alloys, fracture, cleavage, ductile rupture, void growth

#### 1. Introduction

Shape memory alloys (SMAs) are intermetallics with unique properties stemming from a reversible diffusionless solid to solid phase transformation from austenite to martensite [1–6]. Phase transformation may result in large deformations and generation/absorption of heat that impact the fracture response of SMAs along with the reversibility of phase transformation, (re)orientation of martensite variants, overload and TRansformation-Induced Plastic deformation (TRIP) [7–15]. Despite belonging to a relatively brittle class of materials, that of intermetallics, the fracture response of SMAs is characterized by cleavage of specific crystallographic planes with a strong presence of dimples that are indicative of ductile rupture [13, 16, 17]. Ductile rupture involves in general nucleation, growth, and coalescence of microvoids.

Email addresses: jmakkar1004@gmail.com (J. Makkar), tbaxevanis@uh.edu (T. Baxevanis)

<sup>\*</sup>Corresponding author

The existing literature on the fracture response of SMAs deals almost entirely with extrinsic shielding resulting from inelastic deformation left in the wake of the crack. Analytical and numerical analyses of the mechanical fields close to the crack tip [18–26], of the levels of fracture toughness enhancement as a function of transformation metrics [27–30], and of the role of transformation-induced contraction [31], latent heat effects [32, 33], and reversibility of phase transformation [27, 30, 34, 35] in the fracture resistance of SMAs have been reported in literature. Recently, it has been observed that large-scale phase transformation resulting from temperature changes, i.e., cooling, may also promote crack advance [36–39]. These numerical investigations are based on either (i) Linear Elastic Fracture Mechanics (LFEM) tools, assuming that the mechanical fields in the near-tip region are dictated by a linear elastic response, such as the virtual crack closure technique [29, 36], (ii) on cohesive elements, which essentially couple a fracture process model to the stress and strain field of a growing crack [27, 28], or (iii) specialized finite element methods for steady state crack growth based on the path independence of the *I*-integral in such conditions [30, 32, 34]. These, so-called "qlobal", approaches do not pay attention to the failure micromechanisms and have been proven inadequate to describe the fracture of structural metals in many cases of complex loading conditions involving large-scale vielding, mixed-mode cracking, or non-isothermal loading, and for capturing size effects. By way of contrast, the "local" approaches to fracture aim at predicting the fracture toughness of specimens or the fracture load of components on micromechanistical grounds [40–43].

Void formation/growth/coalescence and cleavage are in general intrinsic damage mechanisms promoting crack advance. In addition to phase transformation, the presence of precipitates in large volume fractions, which act as void initiation sites, is another clear differentiator of SMAs from other intermetallics. Ni-rich NiTi alloys are generally heat treated to produce metastable  $Ni_4Ti_3$  precipitates, of large volume fractions, which have been estimated around  $2 \sim 7\%$  depending on aging [44]. Large second phases are also present in both Ti-rich (NiTi<sub>2</sub>/Ni<sub>2</sub>Ti<sub>4</sub>O<sub>x</sub>-type) and Ni-rich (TiNi<sub>3</sub>-type) compositions. Decreasing Ni<sub>4</sub>Ti<sub>3</sub> precipitate size results in a less "ductile" response and a weaker presence of dimples in the fracture surface of SMAs [16]. Similar is the effect of decreasing grain size [45]. Both have been attributed to a strengthening of the matrix against dislocation plasticity. In an effort to examine the role of stress triaxiality on the ductility of SMAs at fracture, Olsen et al. [17] performed experiments on notched round-bars. Similarly to ductile structural metals, the higher the triaxiality, the lower the fracture strain measured. However, in contrast to most ductile structural metals, no evidence of the characteristic cup-and-cone fracture surface or penny-shaped cracks on smooth or mildly notched specimens was observed. The fracture response, although ductile in terms of relatively large fracture strains, was characterized by cleavage with a strong presence of microvoids initiated from inclusions and precipitates.

Fractography, stress–strain, and R-curves alone cannot yield information on the relative importance of the fracture modes or any information about the material deformation response prior to failure. Thus, numerical simulations should be employed to assist experiments in gaining a further insight into the mechanisms that drive fracture in SMAs. Olsen et al. [17] resorted to the Rice–Tracey void-growth model [46] to justify the experimental indications that macroscopic fracture initiation is stress-controlled and starts at the notch-root, i.e., coalescence of voids results from cleavage fracture rather than plastic collapse of the intervoid ligament. Similarly, Bahrami et al. [47, 48] developed a constitutive model that accounts for void growth in the realm of the Gurson–Tvergaard–Needleman model [49–51], which assumes a stress-triaxiality dependence on the strain and void-volume fraction evolution in order to simulate experimental

results. Both the aforementioned models a priori assume that void growth has a strong influence on the fracture response of SMAs and that plastic deformation is the dominant mechanism contributing to void growth.

In contrast to the aforementioned studies, the objective of the present paper is to investigate void growth and coalescence in precipitation-hardened SMAs by unit cell simulations and, by comparison to the available experimental data, draw conclusions on their importance on the fracture response of these materials. Pioneered by Koplik and Needleman [52], numerical investigations of unit cells have been a useful tool to investigate void initiation, growth, and coalescence in the mesoscale [53? -57]. The unit cell consists of a single void, assumed to have originated from a second phase particle. The constitutive response of the surrounding matrix includes phase transformation and plastic deformation. The deformation history prior to void nucleation and its potential effect on microstructure evolution are ignored, *i.e.*, no void nucleation is taken into account, and, thus, only void growth and coalescence are studied.

# 2. Problem Formulation

#### 2.1. Constitutive Response

The constitutive law can describe the isothermal response of SMAs in a temperature range at which the initially stable austenite state fully transforms to martensite upon loading prior to deforming plastically at higher load levels (Figure 1). The isothermal assumption is valid for a range of strain rates within the regime of quasistatic processes. For higher loading rates, the generation of heat during phase transformation from austenite to martensite may result in strong thermomechanical coupling, which is not accounted for herein for simplicity [58, 59].

The constitutive law is based on the Eulerian logarithmic (Hencky) strain [60], its conjugate Kirchhoff stress, the objective logarithmic time rate [61, 62], and the additive decomposition of total stretching (or rate of deformation) into elastic, transformation, and plastic parts. The numerical implementation of the model is based on an *incrementally objective* algorithm in which the evolution equations of the tensorial state variables described below are mapped and integrated in a local configuration and subsequently the discrete equations are mapped back to the Eulerian description [63, 64]. The constitutive model and its numerical implementation have been verified and benchmarked in [64, 65].

#### 2.1.1. Kinematics

The Hencky strain

$$h_{ij} = \frac{1}{2} \ln \left( b_{ij} \right) = \sum_{\alpha=1}^{m} \ln \left( \lambda^{\alpha} b_{ij}^{\alpha} \right), \tag{1}$$

is introduced as the logarithmic measure of the left Cauchy-Green deformation tensor with components  $b_{ij}$ , where  $\lambda^{\alpha}$  are the m distinct eigenvalues of  $b_{ij}$ ,  $b_{ij}^{\alpha}$  are the components of the corresponding eigenvectors, and i, j = 1, 2, 3.

The objective logarithmic time rate of the Hencky strain

$$\mathring{h}_{ij} = \dot{h}_{ij} + h_{im}\Omega_{mj} - \Omega_{im}h_{mj} = D_{ij}, \tag{2}$$

yields the total stretching,  $D_{ij}$ , where  $\Omega_{ij} = W_{ij} + \sum_{\alpha \neq \beta}^{n} \left( \frac{1 + (\lambda^{\alpha}/\lambda^{\beta})}{1 - (\lambda^{\alpha}/\lambda^{\beta})} + \frac{2}{\ln(\lambda^{\alpha}/\lambda^{\beta})} \right) b_{im}^{\alpha} D_{mn} b_{nj}^{\beta}$ ,  $W_{ij}$  are the components of the spin tensor, and "·" denotes material time rate.

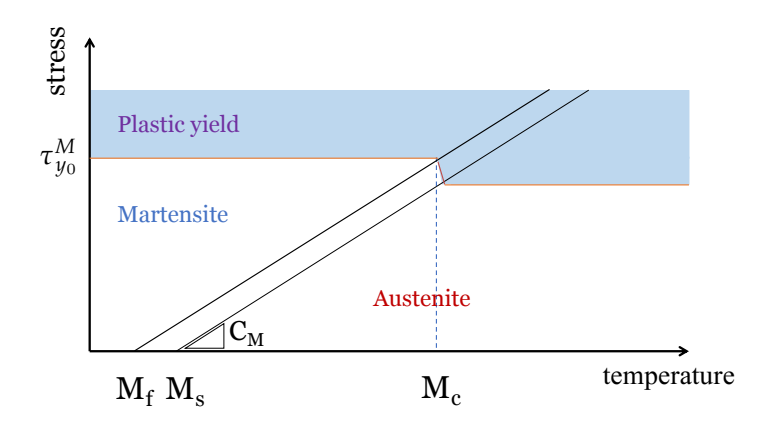


Figure 1: Stress-temperature phase diagram. The model can describe the isothermal response of SMAs in the temperature range  $M_s < T < M_c$  at which the material, initially in the austenite state, fully transforms to martensite before deforming plastically at yield stress  $\tau_{y_0}^M$ .  $M_s$  and  $M_f$  are the martensite-start and martensite-finish temperatures, respectively.

The logarithmic rotations, defined from the differential equation

$$\dot{R}_{ij} = \Omega_{im} R_{mj}, \quad R_{ij}|_{t=0} = \delta_{ij}, \tag{3}$$

define a locally rotating coordinate system in which the material time rates of the rotated (Langrangean) tensors are objective, *i.e.*,

$$\overline{R_{im}a_{mn}R_{jn}} = R_{im}\mathring{a}_{mn}R_{jn} \tag{4}$$

holds, where  $a_{ij}$  are the components of an arbitrary tensor.

Time integration of (4), assuming  $a_{ij} = h_{ij}$  and  $h_{ij}|_{t=0} = 0$  for all i and j, yields

$$h_{ij} = R_{mi} \left( \int_0^t R_{mk} \mathring{h}_{kl} R_{nl} dt \right) R_{nj} \stackrel{(2)}{=} R_{mi} \left( \int_0^t R_{mk} D_{kl} R_{nl} dt \right) R_{nj}, \tag{5}$$

and, thus, additive decomposition of  $D_{ij}$  into elastic, transformation, and plastic parts yields an additive decomposition of the Hencky strain

$$h_{ij} = h_{ij}^e + h_{ij}^{tr} + h_{ij}^p, (6)$$

where  $h_{ij}^e$ ,  $h_{ij}^{tr}$ , and  $h_{ij}^p$  stand for the components of the elastic, transformation, and plastic small strain tensors, respectively.

# 2.1.2. Elastic deformation and phase transformation

Assuming that phase transformation is a volume preserving process, the objective rate of the transformation strain tensor is taken as

$$\mathring{h}_{ij}^{tr} = \dot{\xi} H N_{ij}, \tag{7}$$

where the martensite volume fraction,  $\xi$ , is restricted by  $0 \le \xi \le 1$ , H is the measure of the effective transformation strain when  $\xi = 1$ , *i.e.*,  $H = \sqrt{\frac{2}{3}h_{ij}^{tr}h_{ij}^{tr}}$ , and the flow direction

for transformation,  $N_{ij}$  ( $||N_{ij}|| = 1$ ), depends on the deviatoric Kirchhoff stress tensor, with components  $\tau'_{ij} = \tau_{ij} - \frac{\tau_{kk}}{3} \delta_{ij}$  ( $\tau_{ij} = J\sigma_{ij}$ , where J is the Jacobian of the deformation, and  $\sigma_{ij}$  are the components of the Cauchy stress tensor).

The transformation direction

$$N_{ij} = \frac{3}{2} \frac{\tau'_{ij}}{\bar{\tau}},\tag{8}$$

is the normal to the transformation function

$$\Phi(\tau_{ij}, \xi) = \pi - Y \le 0, \tag{9}$$

where

$$\pi = H\bar{\tau} + \frac{1}{2}\tau_{ij}\Delta S_{ijkl}\tau_{kl} + \rho\Delta s_0 T - \Delta u_0 - \frac{1}{2}a_1\left[1 + \xi^{n_1} - (1 - \xi)^{n_2}\right] - a_2, \tag{10}$$

is the thermodynamic force conjugate to martensite volume fraction, Y > 0 the critical value for the activation of transformation,  $s_0$  and  $u_0$  are the specific entropy and internal energy, respectively,  $\rho$  is the density,  $\Delta$  denotes the difference in property between the martensitic and the austenitic states,  $\bar{\tau} = \sqrt{\frac{3}{2}\tau'_{ij}\tau'_{ij}}$  stands for the effective Kirchhoff stress.  $S_{ijkl} = (1 - \xi)S^A_{ijkl} + \xi S^M_{ijkl}$ , is the effective compliance tensor evaluated by the rule of mixtures, where  $S^A_{ijkl}$  and  $S^M_{ijkl}$  are the components of the compliance tensor of austenite and martensite, respectively, assumed isotropic, i.e.,  $S^{\alpha}_{ijkl} = \frac{1+\nu_{\alpha}}{2E_{\alpha}}(\delta_{il}\delta_{jk} + \delta_{ik}\delta_{jl}) - \frac{\nu_{\alpha}}{E_{\alpha}}\delta_{ij}\delta_{kl}$ , where  $E_{\alpha}$ ,  $\nu_{\alpha}$  denote the Young modulus and Poisson ratio, respectively, and the index  $\alpha$  stands for A in the case of austenite and for M in the case of martensite. The various model parameters introduced above are given in terms of the common material properties that are used to calibrate the constitutive models of SMAs, H,  $M_s$ ,  $M_f$ , and  $C_M$ , where  $C_M$  is the Clapeyron slope for forward transformation (Figure 1). The exponents  $n_1$  and  $n_2$  are chosen to best fit the observed transformation-induced hardening response. The calibration procedure is described in detail in [64]. The relations between the material and model parameters are given in Table 1.

Table 1: Connection between model parameters and the material parameters.

$$\rho \Delta s_0 = -HC^M$$

$$\rho \Delta u_0 = \rho \Delta s_0 M_s$$

$$a_1^t = \rho \Delta s_0 (M_f - M_s)$$

$$a_2^t = -Y$$

#### 2.1.3. Plastic deformation

During plastic deformation of martensite, the objective plastic strain rate is given by

$$\mathring{h}_{ij}^{p} = \bar{h}^{p} \frac{3}{2} \frac{\tau_{ij}'}{\bar{\tau}},$$
(11)

where  $\dot{\bar{h}}^p = \sqrt{\frac{2}{3}\dot{h}^p_{ij}\dot{h}^p_{ij}}$  is the effective plastic strain rate, and the stress state satisfies the consistency condition, which is defined by the von Mises yield surface

$$f(\tau_{ij}, \bar{h}^p) = \bar{\tau} - \tau_y^M = 0.$$
 (12)

Table 2: Parameter values used for the numerical results presented.

parameter	value	parameter	value
$E_A$ [MPa]	62000	Н	0.03
$E_M$ [MPa]	22000	$M_f$ [ $^{o}$ C]	-33
$\nu_A = \nu_M$	0.33	$M_s$ [ $^o$ C]	-27
$\tau_{y_0}^M$ [MPa]	800	$C_M [MPa {}^{o}C^{-1}]$	6
$\lambda$	1500	$n_1 \& n_2$	0.9
n	0.33		

Assuming isotropic hardening, the yield stress  $\tau_{y}^{M}$  evolves as

$$\tau_y^M(\bar{h}^p) = \tau_{y_0}^M + \lambda \left(\bar{h}^p\right)^n, \tag{13}$$

where n and  $\lambda$  are fitting parameters, and  $\bar{h}^p = \int d\bar{h}^p$  is the accumulated equivalent plastic strain.

# 2.2. Unit Cell Model

The axisymmetric void unit cell model, initially employed to investigate ductile fracture in elastic-plastic materials [52], is adopted. The unit cell is cylindrical, with initial length  $2L_{z0}$  and diameter  $2L_{r0}$ , containing a spheroidal void at its center, with initial radii  $r_{z0}$  and  $r_{r0}$ . 248 four-node, linear axisymmetric finite elements (CAX4) are used for the discretization of one quarter of the axisymmetric cross section (Figure 2).

The boundary conditions constrain the cell external boundaries to remain straight and the stress triaxiality

$$T = \frac{\Sigma_m}{\Sigma_e} = \frac{1}{3} \left( \frac{1 + 2\rho}{1 - \rho} \right),\tag{14}$$

to remain constant, where

$$\Sigma_m = \frac{1}{3}(\Sigma_{zz} + 2\Sigma_{rr}), \quad \Sigma_e = |\Sigma_{zz} - \Sigma_{rr}|, \tag{15}$$

stand for the volume-averaged mean and effective Cauchy stress, respectively, and  $\rho = \Sigma_{zz}/\Sigma_{rr}$ . The volume-averaged mesoscopic stress components  $\Sigma_{zz}$  and  $\Sigma_{rr}$  are calculated from the forces generated in the linearly elastic springs (Figure 2),  $F_z = k \left( u_z^I - u_z^{II} \right)$  and  $F_r = k \left( u_r^I - u_r^{II} \right)$  (k is the stiffness of the springs), respectively, which are constrained to deform such that  $\Sigma_{zz} = \rho \Sigma_{rr}$  (see for details [66]).

The macroscopic effective logarithmic strains,  $E_{zz}$  and  $E_{rr}$ , read as

$$E_{zz} = \ln\left(\frac{L_z}{L_{z0}}\right), \quad E_{rr} = \ln\left(\frac{L_r}{L_{r0}}\right)$$
 (16)

and the effective strain as

$$E_e = \frac{2}{3} |E_{zz} - E_{rr}|. (17)$$

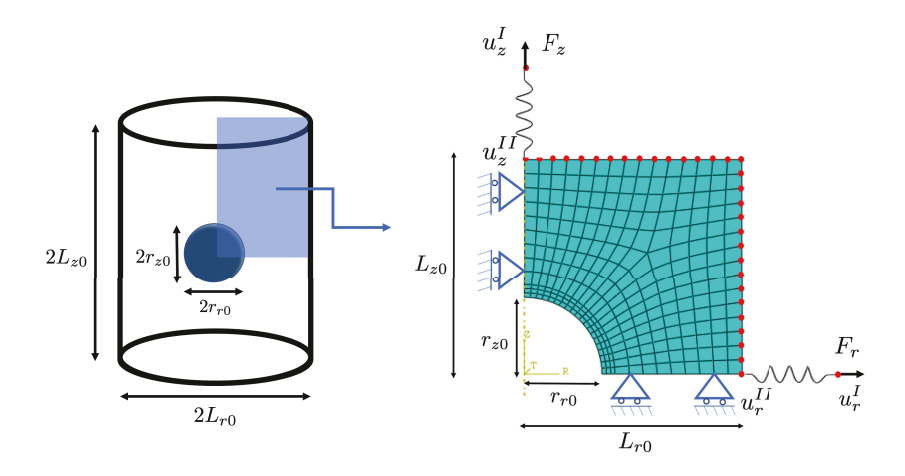


Figure 2: Axisymmetric unit cell and the boundary value problem solved in ABAQUS/STANDARD.

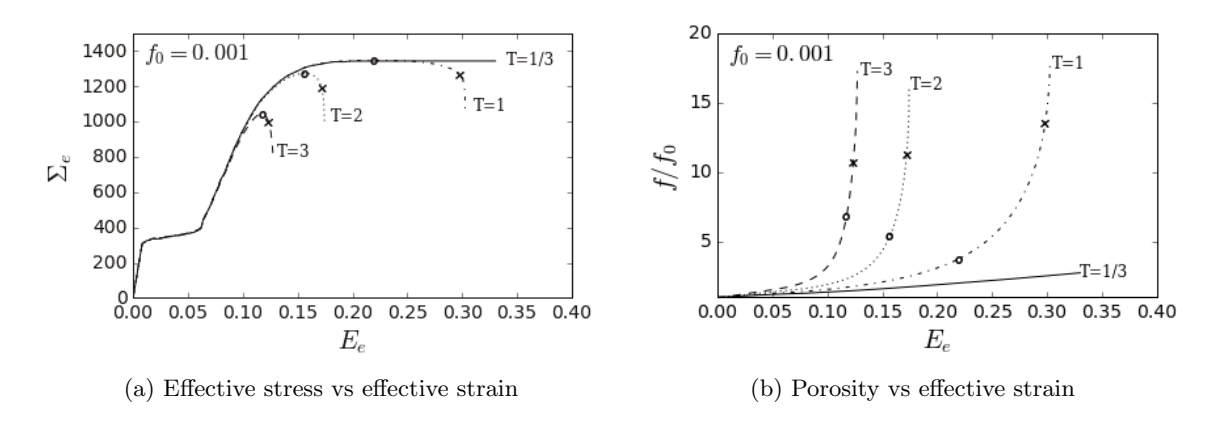


Figure 3: Cell response for  $f_0 = 0.001$ ,  $w_0 = 1$ , and T = 1/3, 1, 2, 3.

## 3. Results & Discussion

The material parameters adopted in the numerical simulations are representative of near-equiatomic, precipitation-hardened NiTi SMAs [67]. The results presented below are at room temperature for three initial porosities,  $f_0 = 2r_{z0}r_{r0}^2/(3L_{z0}L_{r0}^2)$ , set as  $f_0 = 0.001$ ,  $f_0 = 0.03$  or  $f_0 = 0.07$ . The value 0.001 is assumed representative of the volume fraction of large second phase inclusions, such as oxides and carbides, and the values 0.03 and 0.07 representative of the volume fraction of precipitates [44]. In all simulations, the initial cell aspect ratio is set equal to one and the initial void aspect ratio,  $w_0 = r_{z0}/r_{r0}$ , is set as  $w_0 = 1/4$ ,  $w_0 = 1$  or  $w_0 = 4$  to further investigate the effect of the lenticular geometry of precipitates on the cell response. The symbols  $\circ$  and  $\times$  in the figures correspond to the peak value of the volume-averaged effective stress  $\Sigma_e$  and the onset of void coalescence, which corresponds to plastic collapse in the intervoid ligament with elastic unloading away from the localization zone, respectively.

The numerical simulations reveal that void growth/coalescence due to combined phase transformation and plastic deformation proceeds in a manner similar to void growth/coalescence due to plastic deformation alone. At the onset of coalescence, the porosity increases rapidly, the void aspect ratio decreases rapidly, and the load drops abruptly. Coalescence of the voids occurs only

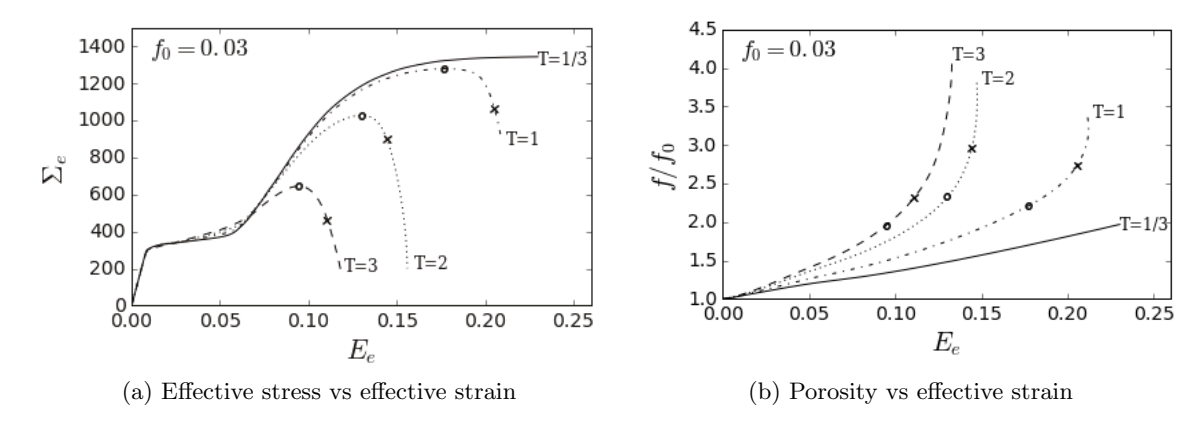


Figure 4: Cell response for  $f_0 = 0.03$ ,  $w_0 = 1$ , and T = 1/3, 1, 2, 3.

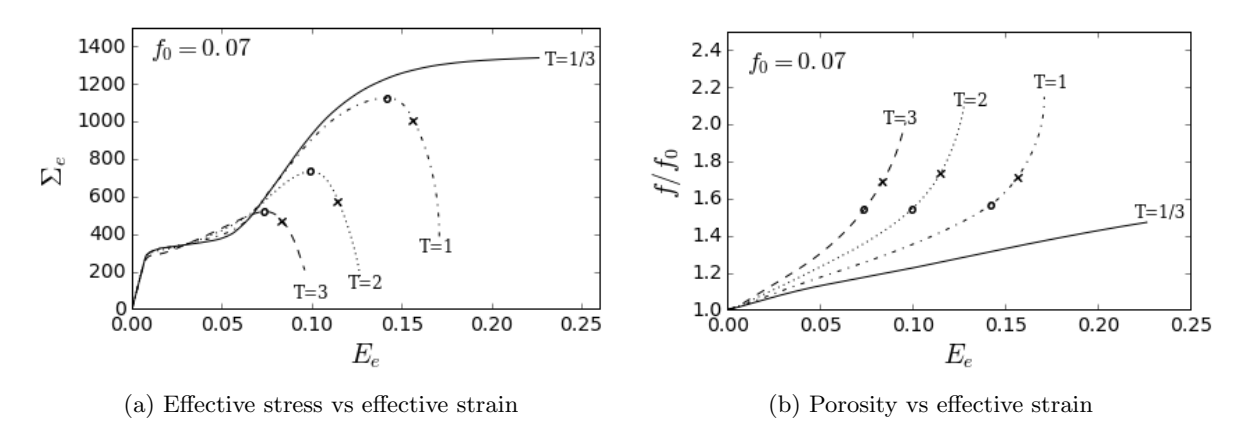


Figure 5: Cell response for  $f_0=0.07,\ w_0=1,\ \mathrm{and}\ T=1/3,1,2,3.$ 

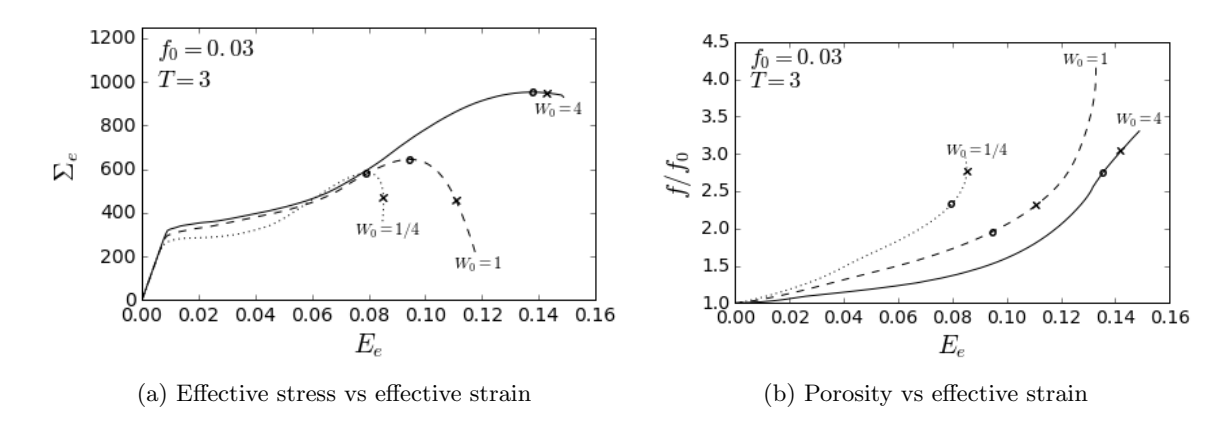


Figure 6: Cell response for  $f_0=0.03,\ w_0=1/4,1,4,$  and T=3.

by plastic localization due to the "finite" nature of the phase-transformation-induced strains. The point of coalescence is always at the descending part of the effective stress—effective strain curve, *i.e.*, past the peak stress points. More importantly for the present study, the strain at the peak volume-averaged effective stress increases with decreasing (i) stress triaxiality (Fig-

ures 3a, 4a, and 5a), (ii) initial porosity (Figures 3a vs 4a vs 5a), and (iii) cell aspect ratio or increasing (iv) plastic hardening and (v) initial aspect ratio for spheroidal voids (small aspect ratio refers to oblate and large aspect ratio to prolate spheroids) (Figure 6a). The ratio of the value of porosity corresponding to the peak stress over the initial porosity,  $f_p/f_0$ , follows the same trends with the exception of triaxiality and aspect ratio of the voids that do not show a monotonic trend (Figures 3b, 4b and 5b, and Figure 6, respectively). These results are in accord with unit cell studies of elastic-plastic materials (see, e.g., [43]); the ones related to the cell aspect ratio and plastic hardening are not presented herein for brevity. The ratio  $f_p/f_0$  is the single most important value on the interpretation of the cell response on the fracture response of SMAs in the discussion below.

As already mentioned, phase transformation and large volume fractions of second phase particles differentiate SMAs from "conventional" intermetallics. Phase transformation has an impact on the  $f_p/f_0$ -value; the higher the transformation strain, the higher the  $f_p/f_0$ -value (Figures 7b and 8b). This impact is dependent on the initial void-volume fraction. The higher the initial void-volume fraction, the lower the effect of phase transformation (Figure 7b vs 8b). A detailed analysis of the combined effect of phase transformation and plastic deformation on the evolution of porosity is omitted here as it is similar to that presented in [57] (Section 3.3), which describes void growth and coalescence in porous elastic-plastic solids with sigmoidal hardening, i.e., materials with a double stage hardening and saturation response; a phenomenological response which is very similar to that of SMAs.

Combining the unit cell studies with the experimental observations in [17], the following hypotheses can be made regarding void growth and coalescence in SMAs.

Void Coalescence.— The available experimental data on notched round-bars indicate that precipitation-hardened SMAs do not exhibit a softening response prior to failure. Given that void coalescence always occurs past the maximum-stress points on the effective stress—effective strain curve, it is reasonable to assume that flow localization in the intervoid ligaments is limited and that void initiation/growth is mostly followed by cleavage.

Void Growth.— Void nucleation aside, assuming that the initial porosity corresponds to the volume fraction of inclusions, the maximum extent of void growth expected can be characterized by the ratio between the porosity value at peak stress and the initial value, i.e.,  $f_p/f_0$ . The porosity that corresponds to the peak stress,  $f_p$ , is dependent on stress triaxiality, cell and void aspect ratio, plastic hardening, transformation characteristics, and initial porosity. The most pronounced dependence is that on the initial porosity,  $f_0$ . The higher the initial porosity,  $f_0$ , the less important the void growth. For  $f_0 = 0.03$ , which is a relatively conservative estimate of the volume fraction of precipitates (around  $2 \sim 7\%$  depending on aging [44]), the numerical results, which are representative of an SMA material (maximum transformation strain  $3 \sim 6\%$ ), show a porosity growth at the peak effective stress value of less than 2.8, i.e.,  $f_p/f_0 < 2.8$  (Figures 4b, 6b, and 8b). Thus, it can be safely assumed that no pronounced void growth is expected in precipitation-hardened SMAs due the high volume fraction of precipitates as compared to conventional ductile materials, in which porosity growth is at least an order of magnitude greater due to the combined effects of (i) their low initial porosities (compared to precipitation-hardened SMAs), and (ii) coalescence.

In conclusion, it is conjectured that void nucleation and cleavage should dominate the fracture response of SMAs due to the high volume fraction of precipitates in SMAs and the limited flow localization observed in experiments [68]. It is expected that the voids first initiate at large second phase particles, such as NiTi<sub>2</sub>, carbides, and oxides [69]. The stress field of the large

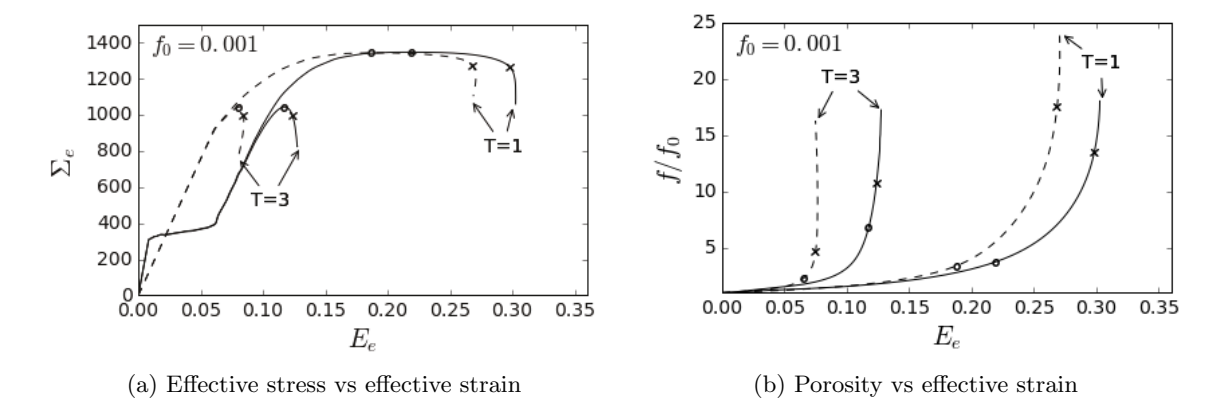


Figure 7: Cell response for  $f_0 = 0.001$ ,  $w_0 = 1$ , and T = 1,3. The solid line corresponds to the SMA and the dashed line to the SMA without accounting for phase transformation, *i.e.*, considering the SMA as an elastic-plastic material with the elastic properties of martensite.

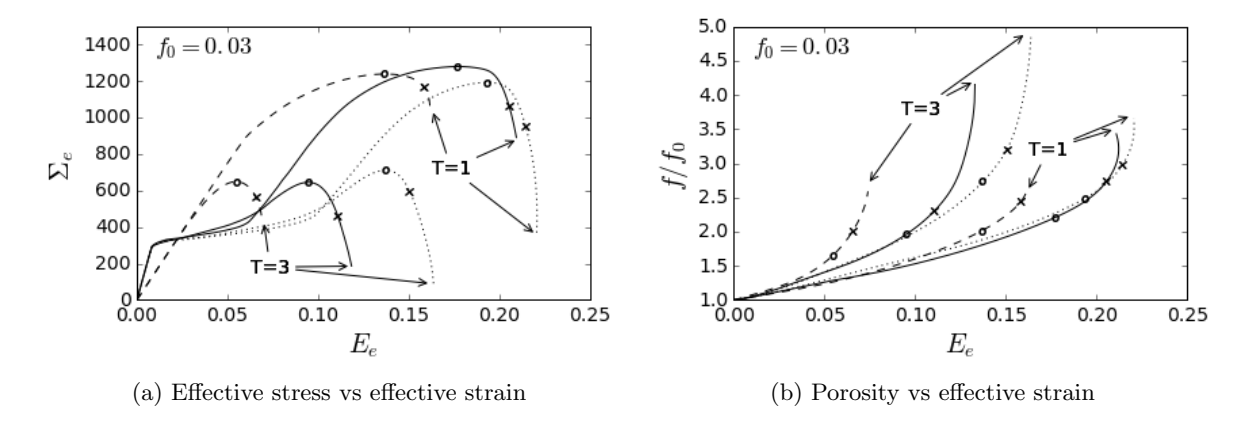


Figure 8: Cell response for  $f_0 = 0.03$ ,  $w_0 = 1$ , and T = 1,3. The solid line corresponds to the SMA, the dashed line to the SMA without accounting for phase transformation, *i.e.*, considering the SMA as an elastic-plastic material with the elastic properties of martensite, and the dotted line to the SMA material with double its maximum transformation strain, *i.e.*, H = 0.06.

voids favors the nucleation of voids from the precipitates [70, 71], which nucleate and grow preferentially near such particles and grain boundaries [72]. However, given the high volume fraction of precipitates as compared to that of larger inclusions (and not the other way around), the distribution of void sizes should not alter significantly the simulated void growth kinetics prior to the peak effective-stress value. Unit cell studies, in the realm of [55, 73–75], are expected to shed light in the void nucleation process, in which phase transformation, contrary to void growth and coalescence, should play a more significant role.

### 4. Summary

Unit cell studies were conducted to study void growth in shape memory alloys in an effort to address the importance of ductile rupture in the overall failure response of these materials. The unit cell consists of a single pre-existing void, assumed to have initiated from a second phase particle, embedded in a SMA matrix material. The numerical simulations, which were repre-

sentative of a near-equiatomic precipitation-hardened NiTi, and experimental evidence, which suggests that the macroscopic crack initiation is stress-driven, indicate that the fracture response is dominated by void initiation and cleavage with void growth playing a secondary/minor role due to the precipitates' high volume fraction.

# Acknowledgements

This study was supported by the US Air Force Office of Scientific Research under Grant No. FA9550-15-1-0287, the National Science Foundation under Grants no. CMMI-1917441, and by NASA-ULI under Grant No. NNX17AJ96A.

## References

- [1] S. Miyazaki. Engineering Aspects of Shape Memory Alloys. Butterworth-Heinemann, London, 1990.
- [2] K. Otsuka and C.M. Wayman, editors. *Shape Memory Materials*. Cambridge University Press, Cambridge, 1999.
- [3] N.B. Morgan. Medical shape memory alloy applications the market and its products. *Mater. Sci. Eng. A*, 378:16–23, 2004.
- [4] D.C. Lagoudas, editor. Shape Memory Alloys: Modelling and Engineering Applications. Springer, New-York, 2008.
- [5] Silvestro Barbarino, EI Saavedra Flores, Rafic M Ajaj, Iman Dayyani, and Michael I Friswell. A review on shape memory alloys with applications to morphing aircraft. *Smart Mater. Struct.*, 23(6):063001, 2014.
- [6] J.M. Jani, M. Leary, A. Subic, and M.A. Gibson. A review of shape memory alloy research, applications and opportunities. *Materials & Design*, 56:1078–1113, 2014.
- [7] G.M. Vasko, P.H. Leo, and T.W. Shield. Prediction and observation of crack tip microstructure in shape memory CuAlNi single crystals. *J. Mech. Phys. Solids*, 50(9):1843–1867, 2002.
- [8] G.M. Loughran, T.W. Shield, and P.H. Leo. Fracture of shape memory CuAlNi single crystals. *Int. J. Solids Struct.*, 40(2):271–294, 2003.
- [9] S.W. Robertson, A. Metha, A.R. Pelton, and R.O. Ritchie. Evolution of crack-tip transformation zones in superelastic Nitinol subjected to in situ fatigue: A fracture mechanics and synchrotron X-ray micro-diffraction analysis. *Acta Mater.*, 55:6198–6207, 2007.
- [10] S. Daly, A. Miller, G. Ravichandar, and K. Bhattacharya. An experimental investigation of crack initiation in thin sheets of nitinol. Acta Mater., 55:6322–6330, 2007.
- [11] M.R. Daymond, M. L. Young, J.D. Almer, and D.C. Dunand. Strain and texture evolution during mechanical loading of a crack tip in martensitic shape-memory NiTi. *Acta Mater.*, 55:3929–3942, 2007.
- [12] A. Creuziger, L.J. Bartol, K. Gall, and W.C. Crone. Fracture in single crystal NiTi. J. Mech. Phys. Solids, 56:2896–2905, 2008.

- [13] S. Gollerthan, M.L. Young, A. Baruj, J. Frenzel, W.W. Schmahl, and G. Eggeler. Fracture mechanics and microstructure in NiTi shape memory alloys. *Acta Mater*, 57:1015–1025, 2009.
- [14] S.W. Robertson, A.R. Pelton, and R.O. Ritchie. Mechanical fatigue and fracture of Nitinol. *Int. Mater. Rev.*, 57(1):1–36, 2012.
- [15] T. Baxevanis and D. C. Lagoudas. Fracture mechanics of shape memory alloys: review and perspectives. *Int. J. Fract.*, 191:191–213, 2015.
- [16] K. Gall, N. Yang, H. Sehitoglu, and Y. I. Chumlyakov. Fracture of precipitated NiTi shape memory alloys. *Int. J. Fract.*, 109:189–207, 1998.
- [17] J.S. Olsen, Z.L. Zhang, H. Lu, and C. van der Eijk. Fracture of notched round-bar NiTi-specimens. *Engng Fract. Mech.*, 84:1 14, 2012.
- [18] S. Yi and S. Gao. Fracture toughening mechanism of shape memory alloys due to martensite transformation. *Int. J. Solids Struct.*, 37:5315–5327, 2000.
- [19] S. Yi, S. Gao, and S. Shen. Fracture toughening mechanism of shape memory alloys under mixed-mode loading due to martensite transformation. *Int. J. Solids Struct.*, 38:4463–4476, 2001.
- [20] G.Z. Wang. Effect of martensite transformation on fracture behavior of shape memory alloy NiTi in a notched specimen. Int. J. Fract., 146:93–104, 2007.
- [21] G.Z. Wang. A finite element analysis of evolution of stress-strain and martensite transformation in front of a notch in shape memory alloy NiTi. *Mater. Sci. Engng. A*, 460–461:460–461, 2007.
- [22] C. Maletta and F. Furgiuele. Analytical modeling of stress-induced martensitic transformation in the crack tip region of nickel-titanium alloys. *Acta Mater.*, 58:92–101, 2010.
- [23] C. Maletta. A novel fracture mechanics approach for shape memory alloys with trilinear stress-strain behavior. *Int. J. Fract.*, 177(1):39–51, 2012.
- [24] T. Baxevanis and D. Lagoudas. A mode I fracture analysis of a center-cracked infinite shape memory alloy plate under plane stress. *Int. J. Fract.*, 175(2):151–166, 2012.
- [25] T. Baxevanis, Y. Chemisky, and D.C. Lagoudas. Finite element analysis of the plane-strain crack-tip mechanical fields in pseudoelastic shape memory alloys. *Smart Mater. Struct.*, 21(9):094012, 2012.
- [26] Gülcan Özerim, Günay Anlaş, and Ziad Moumni. On crack tip stress fields in pseudoelastic shape memory alloys. *Int. J. Fract.*, 212(2):205–217, 2018.
- [27] G. Stam and E. van der Giessen. Effect of reversible phase transformations on crack growth. Mech. Mater., 21:51–71, 1995.
- [28] Y. Freed and L. Banks-Sills. Crack growth resistance of shape memory alloys by means of a cohesive zone model. J. Mech. Phys. Solids, 55:2157–2180, 2007.

- [29] Th. Baxevanis, A. Parrinello, and D.C. Lagoudas. On the fracture toughness enhancement due to stress-induced phase transformation in shape memory alloys. *Int. J. Plast.*, 50:158– 169, 2013.
- [30] T. Baxevanis, C.M. Landis, and D.C. Lagoudas. On the fracture toughness of pseudoelastic shape memory alloys. *J. Appl. Mech. -T ASME*, 81:041005, 2013.
- [31] W. Yan, C.H. Wang, X.P. Zhang, and Y.W. Mai. Effect of transformation volume contraction on the toughness of superelastic shape memory alloys. *Smart Mater. Struct.*, 11:947–955, 2002.
- [32] T. Baxevanis, C.M. Landis, and D.C. Lagoudas. On the effect of latent heat on the fracture toughness of pseudoelastic shape memory alloys. J. Appl. Mech., Transactions ASME, 81(10), 2014. doi: 10.1115/1.4028191.
- [33] Yajun You, Xiaojun Gu, Yahui Zhang, Ziad Moumni, Günay Anlaş, and Weihong Zhang. Effect of thermomechanical coupling on stress-induced martensitic transformation around the crack tip of edge cracked shape memory alloy. *Int. J. of Fract.*, 216(1):123–133, 2019.
- [34] Selcuk Hazar, Wael Zaki, Ziad Moumni, and Gunay Anlas. Modeling of steady-state crack growth in shape memory alloys using a stationary method. *Int. J. Plastic.*, 67:26–38, 2015.
- [35] Dongjie Jiang and Chad M. Landis. A constitutive model for isothermal pseudoelasticity coupled with plasticity. Shape Mem. Super., 2(4):360–370, 2016.
- [36] T. Baxevanis, A. Parrinello, and C.D. Lagoudas. On the driving force for crack growth during thermal actuation of shape memory alloys. *J. Mech. Phys. Solids*, 89:255–271, 2016.
- [37] A. Illiopoulos, J. Steuben, T. Kirk, T. Baxevanis, J. Michopoulos, and C.D. Lagoudas. Thermomechanical failure response of notched NiTi coupons. *Int. J. Solids Struct.*, 125:265–275, 2017.
- [38] S. Jape, T. Baxevanis, and D.C. Lagoudas. Stable crack growth during thermal actuation of shape memory alloys. *Shape Mem. Super.*, 2(1):104–113, 2016.
- [39] S. Jape, T. Baxevanis, and D.C. Lagoudas. On the fracture toughness and stable crack growth in shape memory alloy actuators in the presence of transformation-induced plasticity. *Int. J. Fract.*, 209:117–130, 2017.
- [40] J. Lemaitre. Local approach of fracture. Engng Fract. Mech., 25(5):523–537, 1986.
- [41] A. Pineau. Global and Local Approaches of Fracture Transferability of Laboratory Test Results to Components, pages 197–234. Springer New York, New York, NY, 1992.
- [42] A. Pineau. Development of the local approach to fracture over the past 25 years: Theory and applications. *Int. J. Frac.*, 138(1):139–166, 2006.
- [43] A.A. Benzerga and Jean-Baptiste Leblond. Ductile fracture by void growth to coalescence. In Hassan Aref and Erik van der Giessen, editors, Advances in Applied Mechanics, volume 44 of Advances in Applied Mechanics, pages 169–305. 2010.

- [44] Antonin Dlouhý, Jafar Khalil-Allafi, and Gunther Eggeler. On the determination of the volume fraction of Ni<sub>4</sub>Ti<sub>3</sub> precipitates in binary Ni-rich NiTi shape memory alloys. Zeitschrift fur Metallkunde, 95(6):518–524, 2004.
- [45] Aslan Ahadi and Qingping Sun. Grain size dependence of fracture toughness and crack-growth resistance of superelastic NiTi. *Scripta Mater.*, 113:171–175, 2016.
- [46] J.R. Rice and D.M. Tracey. On the ductile enlargement of voids in triaxial stress fields. J. Mech. Phys. Solids, 17(3):201–217, 1969.
- [47] Hossein Bahrami, S.H. Hoseini, and George Z. Voyiadjis. Fracture analysis of shape memory alloys in martensite and austenite phase based on the voids behavior. *Mech. Mater.*, 137:103119, 2019.
- [48] Hossein Bahrami, S.H. Hoseini, and George Z. Voyiadjis. Fracture investigation of the shape memory alloy using GTN model. *Engng Fract. Mech.*, 216:106519, 2019.
- [49] A. L. Gurson. Continuum Theory of Ductile Rupture by Void Nucleation and Growth: Part I. Yield Criteria and Flow Rules for Porous Ductile Media. *J. Engng Mater. Tech.*, 99(1):2–15, 1977.
- [50] V. Tvergaard. On localization in ductile materials containing spherical voids. Int. J. Fract., 18:237–252, 1982.
- [51] C. Chu and A. Needleman. Void nucleation effects in biaxially stretched sheets. J. Engng Mat. Techn., 102:249–256, 1980.
- [52] J. Koplik and A. Needleman. Void growth and coalescence in porous plastic solids. Int. J. Solids Struct., 24(8):835–853, 1988.
- [53] B. Budiansky, J.W. Hutchinson, and S. Slutsky. Void growth and collapse in viscous solids. In H.G. Hopkins and M.J. Sewell, editors, *Mech. Solids*, pages 13–45. Pergamon, Oxford, 1982.
- [54] S.M. Keralavarma, S. Hoelscher, and A.A. Benzerga. Void growth and coalescence in anisotropic plastic solids. Int. J. Solids Struct., 48(11):1696–1710, 2011.
- [55] N.A. Fleck, J.W. Hutchinson, and V. Tvergaard. Softening by void nucleation and growth in tension and shear. J. Mech. Phys. Solids, 37(4):515–540, 1989.
- [56] Balaji Selvarajou, Shailendra P. Joshi, and A. Amine Benzerga. Void growth and coalescence in hexagonal close packed crystals. J. Mech. Phys. Solids, 125:198–224, 2019.
- [57] Padmeya P. Indurkar and Shailendra P. Joshi. Void Growth and Coalescence in Porous Plastic Solids With Sigmoidal Hardening. J. Appl. Mech., 86(9), 2019.
- [58] J. Shaw and S. Kyriakides. Thermomechanical aspects of NiTi. Journal of the Mechanics and Physics of Solids, 43(8):1243–1281, 1995.
- [59] G. Eggeler, E. Hornbogen, A. Yawny, A. Heckmann, and M. Wagner. Structural and functional fatigue of NiTi shape memory alloys. *Materials Science and Engineering: A*, 378(1):24–33, 2004.

- [60] Heinrich Hencky. Uber die form des elastizitatsgesetzes bei ideal elastischen stoffen. Zeit. Tech. Phys., 9:215–220, 1928.
- [61] WD Reinhardt and RN Dubey. Eulerian strain-rate as a rate of logarithmic strain. Mech. Res. Com., 22(2):165–170, 1995.
- [62] H Xiao, OT Bruhns, and A Meyers. Logarithmic strain, logarithmic spin and logarithmic rate. *Acta Mech.*, 124(1-4):89–105, 1997.
- [63] J.C. Simo and T.J.r. Hughes. Computational Inelasticity. Springer-Verlag, 1998.
- [64] Mengqian Zhang and Theocharis Baxevanis. An Extended 3D Finite Strain Constitutive Model for Shape Memory Alloys. 2020. submitted.
- [65] L. Xu, T. Baxevanis, and D.C. Lagoudas. A three-dimensional constitutive model for the martensitic transformation in polycrystalline shape memory alloys under large deformation. *Smart Mater. Struct.*, 28(7):074004, 2019.
- [66] OP Sovik. Numerical modeling of ductile fracture: A damage mechanics approach. PhD thesis, NTNU: Norwegian University of Science and Technology, 1998.
- [67] AL McKelvey and RO Ritchie. Fatigue-crack growth behavior in the superelastic and shape-memory alloy nitinol. *Metal. Mater. Trans. A*, 32(3):731–743, 2001.
- [68] Tamas Ungár, Jan Frenzel, Susanne Gollerthan, Gábor Ribárik, Levente Balogh, and Gunther Eggeler. On the competition between the stress-induced formation of martensite and dislocation plasticity during crack propagation in pseudoelastic niti shape memory alloys. J. Mater. Res., 32(23):4433-4442, 2017.
- [69] M Karlík, P Haušild, J Adámek, J Drahokoupil, P Novák, and L Perrière. Microstructure of Ni-48 at.% Ti Alloy Prepared from Powder and by Conventional Metallurgy. Acta Phys. Polonica, A., 134(3), 2018.
- [70] JW Hancock and AC Mackenzie. On the mechanisms of ductile failure in high-strength steels subjected to multi-axial stress-states. *Journal of the Mechanics and Physics of Solids*, 24(2-3):147–160, 1976.
- [71] Viggo Tvergaard. Interaction of very small voids with larger voids. *International Journal of Solids and Structures*, 35(30):3989–4000, 1998.
- [72] Peter Filip and Karel Mazanec. On precipitation kinetics in TiNi shape memory alloys. Scripta Mater., 45(6):701–707, 2001.
- [73] A. Needleman. A Continuum Model for Void Nucleation by Inclusion Debonding. J. Appl. Mech., 54(3):525–531, 1987.
- [74] M. Kuna and D. Z. Sun. Three-dimensional cell model analyses of void growth in ductile materials. *Inter. J. Fract.*, 81(3):235–258, 1996.
- [75] Karine Siruguet and Jean-Baptiste Leblond. Effect of void locking by inclusions upon the plastic behavior of porous ductile solids—I: theoretical modeling and numerical study of void growth. *Int. J Plast.*, 20(2):225–254, 2004.